Calcified cartilage revealed in whole joint by X-ray phase contrast imaging

Ludovic Broche, Bertrand Favier, Hélène Rougé-Labriet, Sabine Drevet, Bernard Lardy, Emmanuel Brun, Benjamin Lemasson

Version of Record: https://www.sciencedirect.com/science/article/pii/S2665913121000315
Manuscript_b84f42059f9879e5d4f951dc751704f8

Calcified cartilage revealed in whole joint by X-ray Phase contrast imaging

Ludovic Broche[1,2], Bertrand Favier[3], Hélène Rougé-Labriet[2,4], Sabine Drevet[3,5], Bernard Lardy[3,6], Emmanuel Brun[2,*], Benjamin Lemasson[1]

[1]Univ. Grenoble Alpes, INSERM, U1216, Grenoble Institut Neurosciences, Grenoble, France
[2]University Grenoble Alpes, Inserm, UA7, STROBE Laboratory, Grenoble, 38000, France
[3]University Grenoble Alpes, GREPI EA7408, Grenoble, 38000,France
[4]Novitom, Grenoble,38000, France
[5]University hospital A. Michallon, Orthogeriatric Unit, Geriatric Department Grenoble,38000, France
[6]University hospital A. Michallon, Biochemical Enzymology and protein laboratory, Grenoble, 38000,France

Abstract

Objective: X-ray Phase Contrast Imaging (PCI) is an emerging modality that will be in the next few years available in a wider range of preclinical set-ups. In this study, we compare this imaging technique with conventional preclinical modalities in an osteoarthritis mouse model.
Method
Phase contrast technique was performed on 6 post-mortem, monoiodoacetate-induced osteoarthritis knees and 6 bilateral control knees. The mice knees were then imaged using magnetic resonance imaging and conventional micro computed tomography. Examples of imaging surrogate markers are reported: local distances within the articular space, cartilage surface roughness, calcified cartilage thickness, number, volume and locations of osteophytes.
Results: Thanks to PCI, we can show in 3D calcified cartilage without contrast agent by a non-invasive technique. The phase contrast images reveal more details than conventional imaging techniques, especially at smaller scales, with for instance a higher number of micro-calcifications detected (57, 314 and 329 for MRI, conventional micro-CT and phase contrast imaging respectively). Calcified cartilage thickness was measured with a significant difference ($p<0.01$) between the control (23.4±17.2µm) and the osteoarthritis induced animal (46.9±19.0µm).
Conclusions: X-ray phase contrast imaging outperforms the conventional imaging modalities for assessing the different tissue types (soft and hard). This new imaging modality seems to bring new relevant surrogate markers for following-up small animal models even for low-grade osteoarthritis

Keywords

X-ray phase contrast Imaging, Calcified Cartilage; 3D markers

Introduction

Osteoarthritis (OA) represents the most widespread osteoarticular disease. It constitutes a growing public health problem, with our aging population and expanding obesity wave. Nowadays it represents the most common cause for disability with consecutive annual health care costs of up to 128 billion dollars in the US[1,2]. New therapeutic and symptomatic options for cartilage diseases have been tested in the past years in animal models and clinical, such as analgesic treatment[3], injection of monoclonal antibody[4–6] or low dose radiotherapy[7]. Imaging modalities are becoming a gold standard to quantify the effectiveness of such therapies. Thus, it is crucial to develop, robust and reproducible joint imaging techniques with a high spatial resolution and sensitive to soft and hard tissues. Current clinical and preclinical imaging modalities have limitations in the detection of early cartilage and bony changes. Indeed, conventional X-ray absorption based Computed Tomography (CT) allows clear visualization of bone tissues but provides reduced sensitivity to soft tissues[8]. Cartilage is indeed poorly visible in conventional micro-CT and it mainly shows advanced and irreversible cartilage degradation resulting in joint space narrowing. Changes in the composition of joint cartilage or soft tissues are usually rather evaluated using Magnetic Resonance Imaging (MRI) using sequences such as ultrashort-TE[9]. Yet, images obtained by MRI struggle to render properly bony changes and microcalcifications[10]. Indeed, MRI cannot so far reach the few microns spatial resolution required to characterize properly microcalcifications. Fluorescence imaging is also used to quantify the distribution of specific chemical elements such as reactive oxygen species but is limited to imaging at the macro scale and in two dimensions[11]

Using a wave approach with X-rays, the refraction index of light element materials can be a thousand times greater than its counterpart the absorption factor for the wavelength in radiology[12]. This induces a much greater contrast for soft tissues with X-ray imaging methods based on the detection of the light refraction or with a wave description the phase[13]. These methods, called Phase Contrast Imaging (PCI) in comparison to the conventional method based on absorption. PCI has a strong correlation with MRI in measuring cartilage thickness and with conventional CT in detecting subchondral bony changes[,14,15]. It is indeed possible to visualize simultaneously and in details the high absorbing tissues like bone, and the low-absorbing tissues like cartilage and soft tissue (synovial membranes, muscles ...) as demonstrated by Horng[16]. Nevertheless, to our knowledge, only a few studies evaluated PCI for to study small animal models albeit being a fast 3D imaging technique, contrast agent independent, in-vivo compatible and with a high special resolution.

The objectives of this study are to present the very first results obtained using PCI on a murine OA model and to evaluate the PCI capability to depict soft and hard tissues of the knee compared to the established preclinical imaging modalities. We also propose several new 3D morphometric surrogate markers with a special focus on articular cartilage, calcified cartilage and osteophytes.

Methods

Overall Protocol

All imaging protocols were done post-mortem on six mice, in which we analyzed both knees ($n_{control}$ = 6, n_{MIA} = 6). The removed knees were formalin fixed, agarose imbedded, and synchrotron phase contrast imaging (PCI) was performed, followed by MRI and conventional x-ray microscopy. Then samples were then sliced for histological analysis.

Animal Manipulation

In accordance with the Directive 2010/63/*EU*, the experiments were performed in an agreed animal facility (C3851610006) evaluated by an Ethical Committee for Animal Welfare and authorized (APAFIS #13792-201802261434542 v3). OA pain model was induced by bilateral single intra-articular injection of monoiodoacetate (MIA-OA, Sigma, Saint Quentin-Fallavier, France) in the knee. Six 6 weeks old C57BL6

female mice (Janvier Labs, France) were anaesthetized by xylazine and ketamine injection (10 and 100 mg/kg), a 0.5 mm skin incision was made over both knee, MIA (0.1 mg/μl, 5μl) or the same volume of phosphate buffer (PBS) for control animals was injected through the infra-patellar tendon perpendicular to the tibia using Hamilton syringe with 25µL capacity and dispensable 0.4 mm diameter needles. Mice received buprenorphine once (0.1mg/kg, sub-cutaneous) for pain management during recovery. Mice were monitored for 10 weeks for obvious locomotor disability by visual observation and Rotarod testing (Bioseb, Vitrolles, France) and then sacrificed. Knees were removed, fixated in 4% formaldehyde for 48h and embedded in PBS with 2 % agarose.

Synchrotron X-ray Imaging

Image acquisition was performed at the biomedical beamline of the ESRF (Grenoble, France). A propagation-based PCI technique was used to enhance contrast in between small density changes by capitalizing on both x-ray absorption and refraction. This imaging technique uses highly coherent radiation, with a long sample to detector distance (11 m) to measure interferences between refracted radiations (see Figure 6). Synchrotron X-ray sources are particularly suited to provide such characteristics, allowing for an acquisition time of 8 min at an isotropic voxel size of $6.1\times6.1\times6.1\mu m^3$. A wiggler source was used to produce broad-spectrum synchrotron radiation. The continuous spectrum was filtered to a 52 keV narrow energy band by a double bent Silicium crystal monochromator. This relatively high energy was chosen as a compromise between contrast, loss of spatial resolution due to streak artefacts caused by phase shifts bigger than a pixel and the very long distance imposed by the beamline configuration at the time of the experiment. Images were recorded with a sCMos camera (PCO edge) with a 2560 × 2160 pixels chip. The projections acquired 11 m away from the sample were brought into focus using the Paganin algorithm[33], the $\frac{\delta}{\beta}$ ratio was set to 1000 (the theoretical value of bone) knowing the setup geometry and the approximate elemental composition of the sample. A total of 2500 projections was acquired to cover the 360 degree.

Magnetic Resonance Imaging

MRI was performed at 9.4T in a horizontal bore magnet (Bruker Biospec 94 / 20 Avance III-HD, Bruker BioSpec, Ettlingen, Germany) at the IRMaGe MRI facility (La Tronche, France) equipped with an helium cooled cryoprobe and a phased-array surface receive coils configuration. A 3D ultra-short echo time (UTE) pulse sequence was acquired (echo time = 0.00813 ms; repetition time = 4.0 ms; flip angle = 5°; acquisition matrix = 300 × 300 × 300, average = 4). Such acquisition allows acquiring a volume of $15\times15\times15mm^3$, at a voxel size of $50\times50\times50\mu m^3$ in 17 min.

Conventional X-ray microtomography

Samples were imaged on a conventional microtomograph (EasyTom XL from RXSolution, Chavanod, France) at the SIMaP- GPM2 lab (Grenoble, France). A conventional microfocus X-ray tube was used, with a maximum high voltage set to 60 kVp coupled with a 127 µm flat panel detector allowing for an acquisition time of 11 min for a 11.1 × 11.1 × 8.8 mm^3 volume at a voxel size of $6.06\mu m^3$. The source spot size was adjusted to be inferior to 5µm. The number of projections was 3600.

Histological Analysis

Samples were paraffin embedded; 4μm slices were cut every 30μm and colored using the Safranin-O Fast-Green technique described by Glasson[17] except that the optimal decalcification time was 48h in 20 % EDTA. Histological images were acquired with a Zeiss Axio Scan slide scanner. The OARSI histological grading system guideline was used to grade the severity of OA[17]. This semi-quantitative scoring system ranged from 0 to 6 (the higher the more severe) and was applied to all four quadrants (score out of 24): medial femur, medial tibia, lateral femur, lateral tibia.

PCI Processing and Analysis

Bone and calcified cartilage structure were segmented using a region-growing algorithm[34]. A morphological opening was then used to remove structures smaller than 3 voxels in diameter[35]. All segmented elements (bone and calcified cartilage), not connected to the tibia, femur, fibula, menisci and patella were labelled as calcifications, for which we reported their number and volumes. The marching

cube algorithm[36] was applied to every segmented structure to generate the polygonal surface meshes. A feature preserving mesh smoothing[37] algorithm was then applied to remove aliasing artifacts. Distance map was calculated from the tibia and femur segmented mesh with a fast-marching algorithm[38]. From the distance map, the surface of maximum distances (i.e. surface for which the tibia and femur are equidistant) was extracted to compute the mean and standard deviation of the interspace. Effective thickness of the dense cartilage structures was characterized for both the tibia and femur using a maximal included ball algorithm through the iMorph software[39]. Using the same regions of interest at the condyle positions, the segmented calcified cartilage where numerically filled with growing spheres to fill up the entire volume. The distribution of all the spheres diameters was then normalized to their total numbers ($n_{sphere} \approx 300$). All the curvature point distribution were recorded with negative value for concave surfaces and positive value for convex surfaces roughness was computed with the VTK library[40].

Statistics

Pairwise comparisons were performed by using independent Student-Newman- Keuls tests on each condyle interspace with the tibia, in between experimental conditions. When both condyles were included in one tested group a Kolmogorov-Smirnov test was applied to consider the distributions bimodality. Asymmetric aperture map distributions were pairwise tested in between conditions using a Man-Whitney test. Finally, a Levene's test was used to test pairwise comparison of the curvature map standard deviations. All statistical tests were carried out with a significance level of $p < 0.01$ using the SciPy statistical library with the Python3.7 language[41,42].

Results

Comparison of the Phase Contrast Imaging technique to MRI, X-ray micro-tomography

Figure 1 shows a representative slice, extracted from each 3D volumes, of a MIA-OA mice knee. MRI (Figure 1A) with a ultra-short echo time (UTE) sequence shows a readable contrast between bone and tissue structure as well as within the tissue structures (tendons, muscles, cartilages). But, the lack of image definition (pixel size of $50\mu m^3$) gives a poor geometric representation of the overall bone, meniscus and tibial ligaments and underestimate the total number of calcifications ($Ncalcification_{MRI} = 57$, $Ncalcification_{CT} = 314$ vs $Ncalcification_{PhaseContrast} = 329$). Due to poor contrast within the bone structure, calcified cartilage, cortical and trabecular bone appear homogeneous with the MRI technique. Conventional X-ray micro-tomography (Figure 1B) with its high resolution shows a precise morphology of the bone structure but completely lacks contrast within soft and bony tissues. PCI (Figure1C) allies a high image precision good differentiation between all anatomical elements of the knee joint (muscle, tendon, calcified cartilage, articular cartilage, bone and calcifications). The insets shown in Figure 1D and E are situated in the joint space and show the same zone with adapted gray scales for enhancing either the articular cartilage and synovial fluid (Figure 1D) or the calcified cartilage (Figure 1E). On these example, one can clearly see, in the same imaging modality, all the element of the knee joint: cartilage, calcified cartilage and chondrocytes. All the imaging dataset for the leg imaged with the different modalities are available at doi://10.17605/OSF.IO/W4P6M.

Validation of PCI results with histological images

To validate our PCI data with the gold standard histology, we present in Figure 2, a comparison on a representative slice of a control (Figure 2A,C,E,G,H) and a MIA-OA (Figure2B,D,F,I,J) mice knees acquired by PCI (Figure2A-D) and safranin-0 colored histological sections (Figure2E-J) with a focus on the medial femoral condyle area (C,D,G-J). To highlight the unique capabilities of PCI to render such contrast, the PCI contrast window was set to highlight the density changes within the calcified structures. The articular cartilage is therefore too dark to be visible and we indicate by a red dotted line its boundaries found thanks to a segmentation based on another contrast windowing (see method section). The distinction between the subchondral bone (†) and the calcified cartilage (∗) can be visualized with PCI on both the control and the MIA slices. Dark rounded dots, visible within the calcified cartilage in PCI are ascribed to chondrocytes (γ). In the knee histological sections, the purple safranin-O stains the cartilage peptidoglycans. The calcified cartilage can be found on these images by a reddish color that seem to be

correlated with the PCI images in both the control and MIA images. In the MIA-treated knee, osteoarthritis is assessed by disorganization and broadening of the cartilage, safranin-O negative areas at the surface (Figure 2I), clefts at the cartilage surface with dead cell ghosts (Figure2J). These features can also be seen on the PCI slices, with a thicker calcified cartilage layer and with darker and larger chondrocytes.

3D histomorphometry analysis of two joints

Figure 3 and Figure 4 show representative examples of the different surrogate markers PCI may provide on both the control and MIA knee joints. After the segmentation of our images in bone and calcified cartilages zones we can measure virtual 3D histomorphometry quantities that are non-accessible with gold standard 2D histology.

The Figure 3 presents rapid and direct 3D measurements of features similar to those used in human X-ray imaging or in histological evaluation of OA. We calculated on our segmented bone structures the mean femur to tibia inter-space at the condyle positions in three dimensions (Figure 3A). The regions of interest where the mean distance and their standard deviation were calculated are indicated by the gray square. It is interesting to note that by averaging the mean inter-distance of both condyles no statistical differences appears in between the Control and the MIA joints (56.7±8.5μm vs 57.4±17.3μm) (Plain color bars in Figure 3D). But the MIA-OA knee displays a destabilization between his two condyles with a thin medial femur/tibia interspace (39.4±7.1μm) and a large lateral femur/tibia interspace (70.3±6.5μm), while such asymmetry is not present on the control knee (54.2±8.5μm vs 58.2±8.5μm).

Thanks to a granulometry algorithm[19], we can calculate in three dimensions the local thickness of the different tissues. The Figure 3B shows on a sagittal cross-section the distribution of the local thickness whilst the Figure 3C represents those values projected in 3D on the segmented surfaces. The full distribution of calcified cartilage thickness in both femur and tibia for each condition is shown in the lower panel E and F. The thickness analysis on the calcified cartilage shows an overall increased in thickness with the MIA-OA knee 46.9±22.4μm compared to the control 23.4±17.2μm thickness. Bone wise, the femur and tibia calcified cartilage mean thickness are 47.6 ± 15.7 μm and 46.3 ± 22.4 μm respectively on the MIA-OA knee, and 28.7 ± 18.6 μm and 18.1 ± 13.9 μm respectively in the control knee. No statistical differences were found in between the femur and tibia on each of the two conditions for this mouse. We can nevertheless note that the local thickness is the largest in the MIA joints within the condyles where the femur/tibia interspace is the smallest. The total volume of MIA calcified cartilage in the full join is also largely superior with $V_{MIA} = 9.42 \times 10^{-2}\ mm^3$ vs $V_{Ctr} = 6.35 \times 10^{-2}\ mm^3$

Additionally, we computed three-dimensional based measurements on the PCI images that are not accessible with histology. We first computed the surface roughness (estimated as the local curvature of a surface) of different interfaces: the calcified cartilage/articular cartilage interface and the calcified cartilage/ subchondral bone interface. The Figure 4A-D shows such measurements where the roughness is projected onto the surfaces (represented in false colors) of both the calcified cartilage (A and C) and subchondral bone (B and D) in an example of control (A and B) and MIA (C and D) joints. The subfigure 4E-H, together with an exemplary image, shows the roughness distributions restricted to the condyles positions. Figure 4E and F is the measurement performed on the femur, and G and H on the tibia. Note that only the femur subchondral bone displays a significant increase in curvature variability on the MIA-OA model (curvature$\sigma_{Curv_{OA}} = 0.143 \mu m^{-2}$; $\sigma_{Curv_{Ctrl}} = 0.075 \mu m^{-2}$).

Figure 4I-L shows the 3D distribution of all the segmented osteophytes in both control (I) and MIA (J) where the osteophytes were colored. Osteophytes were defined as high density elements not connected to the three main bones or the menisci. The graph in Figure 4K and L, shows a 2D projections in sagittal and transverse coordinates where the volume of the osteophytes is schematized by a circle with the same volume. As one can see, the control knee presents some osteophytes probably due to the injection of PBS but the MIA-OA knee displays a significantly higher amount ($n_{OA} = 31$ vs $n_{Ctrl} = 13$) with a larger total volume ($V_{OA} = 4.29 \times 10^{2}$ µL vs $V_{Ctrl} = 6.01 \times 10^{3}$ µL).

Quantification of the whole image database

All the computed metric results are recapitulated in table1. Figure5 displays the comparison of the morphological parameters computed in the same fashion of the above examples on the PCI images but for

the all the MIA injected legs (n = 6) and their controlateral legs (n = 6). Figure 5A presents the mean inter-space distance between femur and tibia taking into account both condyles (bars in plain color). The distance is significantly higher (p-value ≤ 0.01) for the control than for the MIA knees. The group displays the same trend as in the above example when measuring specifically the interspace in between condyles. The same strong destabilization appears in between the MIA medial and lateral condyle (25.6±6.8μm vs 70.7±4.3μm) while in the control group such effect is statistically non relevant (55.6±9.1μm vs 56.7±4.1μm).

The same trend can be observed when measuring the calcified cartilage thickness (Figure 5B and C). The MIA model animals display a significant higher thickness compared to the control for both the femurs (24.2±7.3μm vs 47.7±15.4μm) and the tibia (25.1±8.1μm vs 44.4±17.2μm).

The surfaces roughness at the calcified and articular cartilage interface shows a smooth surface along the control and the MIA group for both the femur and tibia (Figure 5D and F). On the other hand, as shown in Figure 5E and G, the roughness on the tidemark between the calcified cartilage and subchondral bone is significantly different in between the two measured groups with a larger variability in curvature surface for the MIA model for both and tibia.

The calcification distribution is significantly different between the model and the control (nb_{MIA} = 54.8 ± 21.5 vs nb_{Ctr} = 12.1 ± 4.21) (Figure 5H). The volumes distribution seems bimodal in the MIA model with a total of $V_{Ctr} = 2.77 \times 10^{3} \pm 4.26 \times 10^{2}$ µL vs $V_{MIA} = 3.70 \times 10^{4} \pm 6.84 \times 10^{3}$ µL. As expected, the smallest calcifications are mainly distributed in the tightest spaces in between the two condyles.

The total volume of calcified cartilage was also higher in the MIA group compare to the control with a mean volume per animal of $V_{MIA} = 11.0 \pm 2.45 \times 10^{-2}$ mm^3 vs $V_{Ctr} = 5.84 \pm 0.86 \times 10^{-2}$ mm^3

Discussion

The main objective of this work was to study whether Phase Contrast Imaging is a suitable imaging modality for studying at high resolution a murine osteoarthritis model. We demonstrated that compared to conventional MRI and conventional micro CT images, PCI technique has a higher image sensibility and resolution. It allows in a single scan a full representation of the soft and calcified tissue structures at the same resolution than conventional micro-CT that is limited to bone visualization only. We showed for the first time the possibility to distinguish in 3D, using a non-invasive technique i.e. in complete unaltered mice knees, the articular and calcified cartilages as well as the subchondral bone and some clustered chondrocytes.

In this study, for sake of comparison with literature, we used the most characterized chemical-induced OA mouse model based on the injection into the rodent knee joint of mono-iodoacetate (MIA), an inhibitor of glyceraldehyde-3-phosphate dehydrogenase, a glycolysis enzyme[20]. Although not fully depicting the disease progression in human, this MIA-OA model induces chondrocytes cell death within a week, a rapidly evolving OA and formation of osteophytes in rodent[21]. The chemical agents (Mono-Iodo-Acetate (MIA), papain, collagenase) induce very serious lesions with complete and rapid destruction of the cartilage making it impossible to study the early phases of OA disease. Despite that, to depict the joints tissue elements with enough contrast at the micro scale in such a small model remain highly challenging with conventional pre-clinical imaging modalities. In this study the histological lesions are severe and confirm that an OA has been induced. Some samples are close to the maximum of the OARSI scoring system with large depletion of proteoglycan staining, while other have a lack of articular cartilage. Mice calcified cartilage is proportionally larger in mice than in human[17] and mice MIA-OA model is mildly affected by mechanical stress due to the animal weight[20]. We nevertheless found thickening of the calcified cartilage and a rougher surface of the tidemark in the OA-model. As expected on an MIA-OA model[22], we also found a drastic increase in micro-calcification number and volume. Such metrics could potentially be a relevant biomarker to spot early stage of MIA-OA model. On the other hand, surface roughness of the subchondral bone and calcified cartilage tidemarks did not exhibit any pertinent

outcomes on that model. We also observed no sign of subchondral bone alteration such as osteophytes, vascular infiltration or osteoclasts. In a hypothetical clinical usage of the PCI technique for osteoarthritic joint detection, calcified cartilage thickening could potentially join the already existing diagnostic radiographic hallmarks.

The secondary objective of this study was to present some surrogate markers this 3D imaging modality may offer. Besides the measurements of features classically admitted as hallmarks of OA (cartilage thickness, distance between bones), we proposed new morphological biomarkers to grade cartilage alterations, calculated here in 3D. These markers were calculated on the calcified cartilage due to the lack of articular cartilage on some animals of the MIA group, but in principles all these morphological parameters could have been measured on other tissues. In summary, we have shown that synchrotron radiation phase contrast imaging is a promising technique to rapidly detect and quantify microstructures for the investigation of small animal models of osteoarthritis. For example, the mean distance between the tibial plate and the femur is not different between the control and the MIA group but a difference can be observed if one measure separately the condyles. As expected, the calcified cartilage is thicker than in the OA group even in a OA low grade knee. The number and volume of calcifications seem to be a good indicator of the disease. The roughness of the interface between the calcified cartilage and the subchondral bone seem to be discriminant as well contrary to the interface between articular and calcified cartilage.

The main limitation of this study is the low number of investigated samples (n=6). Future studies will be carried out in larger groups of animals and other mouse model (surgically induced for example) to further evaluate the usefulness of PCI discriminant markers in the OA diseases. This limitation is mainly due to the limited access to synchrotron. But as previously shown the PCI technique is perfectly compatible with the preclinical in-vivo applications[23,24]. The next steps will consist in performing such experiment *in-vivo* on laboratory systems at a reduced radiation dose. Indeed synchrotron limited access, does not allow to follow-up the pathologies or at the cost of using many animals; while thanks to recent development performing such experiment on conventional X-ray source seems feasible in relatively short future. Indeed, the technique does not need any sample preparation or chemical injection and the deposited radiation dose could drastically be reduced with iterative reconstruction algorithm[25]. Latest development in PCI techniques using grating interferometry[26–28] has proven the feasibility of performing phase contrast with clinical sources. Unfortunately, in these studies the application of PCI remains in 2D due to the additional optics used. A simple approach using a random modulator[29–31] has recently shown that PCI can be transferred on conventional source with short acquisition time and reduced radiation dose to the sample[32].

To conclude, PCI provides in a single examination, a better and a more detailed depiction of the different tissues of small animal models. The sensitivity of PCI makes possible a diagnosis and staging tool of the joint deterioration to support the development of new pre-osteoarthritic treatments and could in the future be applied to clinical studies.

Author contributions

Study conception and design: LB, BF, HRL, SD, BLa, BLe, EB; Data acquisition: LB, BF, HRL, EB, BLe; Data analysis and interpretation: LB, BLe, EB; Drafting the article: LB, BF, HRL, SD, BLa, BLe, EB; Article final approval: LB, BF, HRL, SD, BLa,BLe, EB.

Acknowledgements

The authors acknowledge the ESRF for granting beamtime and their support during the experiment. Part of this study was funded by the Idex Grenoble grant IRS Valium. The authors acknowledge C. Ferrero for scientific discussion, L. Salvo P. Lhuissier for beamtime and help on the conventional microCT device.

Conflict of Interest.

The authors declare no conflict of interests

References

1. Arden, N. & Nevitt, M. C. Osteoarthritis: Epidemiology. *Best Pract. & Res. Clin. Rheumatol.* 20, 3 – 25, DOI: https://doi.org/10.1016/j.berh.2005.09.007 (2006). Osteoarthritis.

2. Hawker, G. A. Osteoarthritis is a serious disease. *Clin. Exp. Rheumatol* 37, S3–S6 (2019).

3. Stevens, R. M. *et al.* Randomized, double-blind, placebo-controlled trial of intraarticular trans-capsaicin for pain associated with osteoarthritis of the knee. *Arthritis & Rheumatol.* 71, 1524–1533 (2019).

4. Fleischmann, R. *et al.* Upadacitinib versus placebo or adalimumab in patients with rheumatoid arthritis and an inadequate response to methotrexate: Results of a phase iii, double-blind, randomized controlled trial. *Arthritis & Rheumatol.* 71, 1788–1800 (2019).

5. Kloppenburg, M. *et al.* Phase iia, placebo-controlled, randomised study of lutikizumab, an anti-interleukin-1α and anti-interleukin-1β dual variable domain immunoglobulin, in patients with erosive hand osteoarthritis. *Annals rheumatic diseases* 78, 413–420 (2019).

6. Jin, Y. *et al.* Cgrp blockade by galcanezumab was not associated with reductions in signs and symptoms of knee osteoarthritis in a randomized clinical trial. *Osteoarthr. cartilage* 26, 1609–1618 (2018).

7. Minten, M., Mahler, E., den Broeder, A., Leer, J. & van den Ende, C. Ab0864 the efficacy and safety of low-dose radiotherapy on pain and functioning in patients with osteoarthritis: A systematic review (2015).

8. Botter, S. *et al.* Quantification of subchondral bone changes in a murine osteoarthritis model using micro-ct. *Biorheology* 43, 379–388 (2006).

9. Du, J. & Bydder, G. M. Qualitative and quantitative ultrashort-te mri of cortical bone. *NMR Biomed.* 26, 489–506, DOI: 10.1002/nbm.2906 (2013). https://onlinelibrary.wiley.com/doi/pdf/10.1002/nbm.2906.

10. Mohan, G. *et al.* Kartogenin treatment prevented joint degeneration in a rodent model of osteoarthritis: A pilot study. *J. Orthop. Res.* 34, 1780–1789 (2016).

11. Xie, L. et al. Quantitative imaging of cartilage and bone morphology, reactive oxygen species, and vascularization in a rodent model of 11. Xie, L. et al. Quantitative imaging of cartilage and bone morphology, reactive oxygen species, and vascularization in a rodent model of osteoarthritis. Arthritis & Rheum. 64, 1899–1908 (2012).

12. Bravin, A., Coan, P. & Suortti, P. X-ray phase-contrast imaging: from pre-clinical applications towards clinics. Phys. Medicine & Biol. 58, R1–R35, DOI: 10.1088/0031-9155/58/1/R1 (2013).

13. Davis, T., Gao, D., Gureyev, T., Stevenson, A. & Wilkins, S. Phase-contrast imaging of weakly absorbing materials using hard x-rays. Nature 373, 595–598 (1995).

14. Wilkins, S. W., Gureyev, T. E., Gao, D., Pogany, A. & Stevenson, A. W. Phase-contrast imaging using polychromatic hard x-rays. Nature 384, 335–338, DOI: 10.1038/384335a0 (1996).

15. Geith, T. et al. Quantitative assessment of degenerative cartilage and subchondral bony lesions in a preserved cadaveric knee: propagation-based phase-contrast ct versus conventional mri and ct. Am. J. Roentgenol. 1317–1322 (2018).

16. Horng, A. et al. Cartilage and soft tissue imaging using X-rays: propagation-based phase-contrast computed tomography of the human knee in comparison with clinical imaging techniques and histology. Investig. radiology 49, 627–34, DOI: 10.1097/RLI.0000000000000063 (2014).

17. Glasson, S. S., Chambers, M. G., Van Den Berg, W. B. & Little, C. B. The oarsi histopathology initiative 2013; recommendations for histological assessments of osteoarthritis in the mouse. Osteoarthr. Cartil. 18, S17–S23, DOI: 10.1016/j.joca.2010.05.025 (2010).

18. Sethian, J. A. Fast marching methods. SIAM review 41, 199–235 (1999).

19. Brun, E., Ferrero, C. & Vicente, J. Fast granulometry operator for the 3d identification of cell structures. Fundamenta Informaticae 155, 363–372 (2017).

20. Kuyinu, E. L., Narayanan, G., Nair, L. S. & Laurencin, C. T. Animal models of osteoarthritis: classification, update, and measurement of outcomes. J. orthopaedic surgery research 11, 19 (2016).

21. Mapp, P. et al. Differences in structural and pain phenotypes in the sodium monoiodoacetate and meniscal transection models of osteoarthritis. Osteoarthr. cartilage 21, 1336–1345 (2013).

22. Li, G. et al. Subchondral bone in osteoarthritis: insight into risk factors and microstructural changes. Arthritis research &therapy 15, 223 (2013).

23. Bech, M. et al. In-vivo dark-field and phase-contrast x-ray imaging. Sci. reports 3, 3209 (2013).

24. Fardin, L. et al. Enhancing lung tumor visibility using in-vivo analyzer-based x-ray phase contrast imaging in mouse: A feasibility study. Am. J. Respir. Critical Care Medicine 195 (2017).

25. Zhao, Y. et al. High-resolution, low-dose phase contrast X-ray tomography for 3D diagnosis of human breast cancers. Proc. Natl. Acad. Sci. United States Am. 109, 18290–18294, DOI: 10.1073/pnas.1204460109 (2012).

26. Pfeiffer, F. et al. Grating-based x-ray phase contrast for biomedical imaging applications. Zeitschrift für medizinische Physik 23, 176–185 (2013).

27. Yoshioka, H. et al. Imaging evaluation of the cartilage in rheumatoid arthritis patients with an x-ray phase imaging apparatus based on talbot-lau interferometry. Sci. Reports 10, 1–9 (2020).

28. Wang, Z. et al. Non-invasive classification of microcalcifications with phase-contrast x-ray mammography. Nat. communi- cations 5, 1–9 (2014).

29. Paganin, D. M., Labriet, H., Brun, E. & Berujon, S. Single-image geometric-flow x-ray speckle tracking. Phys. Rev. A 98, 053813, DOI: 10.1103/PhysRevA.98.053813 (2018).

30. Labriet, H. et al. 3d histopathology speckle phase contrast imaging: from synchrotron to conventional sources. In Medical Imaging 2019: Physics of Medical Imaging, vol. 10948, 109481S (International Society for Optics and Photonics, 2019).

31. Zdora, M.-C. et al. X-ray phase-contrast imaging and metrology through unified modulated pattern analysis. Phys. review letters 118, 203903 (2017).

32. Rougé-Labriet, H. et al. Comparison of x-ray speckle based imaging deflection retrieval algorithms for the optimization of radiation dose. Phys. Medicine & Biol. (2020).

33. Paganin, D., Mayo, S. C., Gureyev, T. E., Miller, P. R. & Wilkins, S. W. Simultaneous phase and amplitude extraction from a single defocused image of a homogeneous object. J. Microsc. 206, 33–40, DOI: 10.1046/j.1365-2818.2002.01010.x (2002).

34. Adams, R. & Bischof, L. Seeded region growing. IEEE Transactions on pattern analysis machine intelligence 16, 641–647 (1994).

35. Asano, A., Kobayashi, Y., Muraki, C. & Muneyasu, M. Optimization of gray scale morphological opening for noise removal in texture images. In The 2004 47th Midwest Symposium on Circuits and Systems, 2004. MWSCAS'04., vol. 1, I–313 (IEEE, 2004).

36. Rajon, D. & Bolch, W. E. Marching cube algorithm: review and trilinear interpolation adaptation for image-based dosimetric models. Comput. Med. Imaging Graph. 27, 411–435 (2003).

37. Jones, T. R., Durand, F. & Desbrun, M. Non-iterative, feature-preserving mesh smoothing. In ACM SIGGRAPH 2003 Papers, 943–949 (2003).

38. Man, D., Uda, K., Ueyama, H., Ito, Y. & Nakano, K. Implementations of a parallel algorithm for computing euclidean distance map in multicore processors and gpus. Int. journal networking computing 1, 260–276 (2011).

39. Brun, E., Vicente, J., Topin, F. & Occelli, R. Imorph: A 3d morphological tool to fully analyse all kind of cellular materials. Cell. Met. for Struct. Funct. Appl. (2008).

40. Will Schroeder, B. L., Ken Martin. Visualization Toolkit: An Object-Oriented Approach to 3D Graphics, 4th Edition (Kitware, 1996).

41. Falissard, B. Comprendre et utiliser les statistiques dans les sciences de la vie ((DEPRECIATED), 2005).

42. Virtanen, P. et al. Scipy 1.0: fundamental algorithms for scientific computing in python. Nat. methods 17, 261–272 (2020).

Figure 1. Representative images of one osteoarthritis knee sample observed by each imaging technique: A:MRI with a ultra-short echo time sequence (echo time = 0.00813 ms; repetition time = 4.0 ms; flip angle = 5°; voxel size=50 × 50 × 50 μm^3), B: Conventional X-ray micro-tomography Image (Source voltage = 60 kVp; voxel size =6.06 × 6.06 × 6.06 μm^3) and C: Synchrotron X-ray phase contrast imaging (source energy = 52 keV; voxel size = 6.1 × 6.1 × 6.1 μm^3), D,E: Phase contrast Image magnification with a soft (D) and hard (E) tissue contrast window.

Figure 2. Representative images acquired by PCI (A-D) and their corresponding histological slices (E-J) of the control (A,C,E,G,H) and the MIA-OA model (B,D,F,I,J). Magnified images of the lateral condyle (yellow and black square) highlight the subchondral bone (†), calcified cartilage (*), uncalcified cartilage (red dotted line) and example of chondrocytes (γ)

Figure 3. Quantification of the knee joint interspace and calcified cartilage thickness. A and D : Computed inter-space between the condyles contact points and tibia (gray squares) on both control and MIA-OA model. Bars chart show the mean value and standard deviation of all calculated inter-spaces (*: $p < 0.01$). B and C: Computed calcified cartilage thickness for control and MIA-OA model, with B a representative cross section and C the 3D distribution of local thickness. E and F : distribution of all calculated thickness in on the femur (E) and the tibia (F) (*: $p < 0.01$).

Figure 4. Quantification of knees structures roughness and calcifications. A-H: Computed roughness of the surface linemark between the calcified cartilage and cartilage (A and C) and Subcondral bone and calcified cartilage (B and D). A and D: 3D mapping of the calculated roughness E-H: Roughness Distribution calculated in between the two condyles in the Femur (E and F) and Tibia (G and H) I-J: Quantification of all the labeled calcifications . I and J: 3D rendering of the detected calcification, on the control knee (I) and MIA (J). K-L: 2D representation of all the condrocite coronaly projected with surface area the volume of each condrocites.

Figure 5. Quantification of knees structures morphology. Comparison made on the MIA model (n=6) and the controlateral legs (n=6). A : Computed mean and standard deviation inter-space between the condyles contact points and tibia (*: $p < 0.01$). B and C Histogram of the thickness of the calcified cartilage for the femurs and the tibias. D, E, F, G: Computed surface roughness on the calcified/uncalcified cartilage tidemark (D and F) and subchondral bone/calcified cartilage tidemark (E and G). H: Representation of the location and the number of calcifications (up) with their volume distribution (bottom).

Figure 6. Experimental set up of the X-ray Phase Contrast Image A wiggler source produced a broad-spectrum synchrotron ration which was filtered to a narrow energy band at 52 keV by a double bent Silicium crystal. Sample was 11 meters from the detector in order to broaden x-ray interference. A gadolinium oxysulfide phosphor screen was used as scintillator to convert the x-ray to visible light. Images in visible light were then recorded indirectly by a sCMOS camera coupled with an optical system giving a voxel size of 6.1×6.1×6.1μm^3.

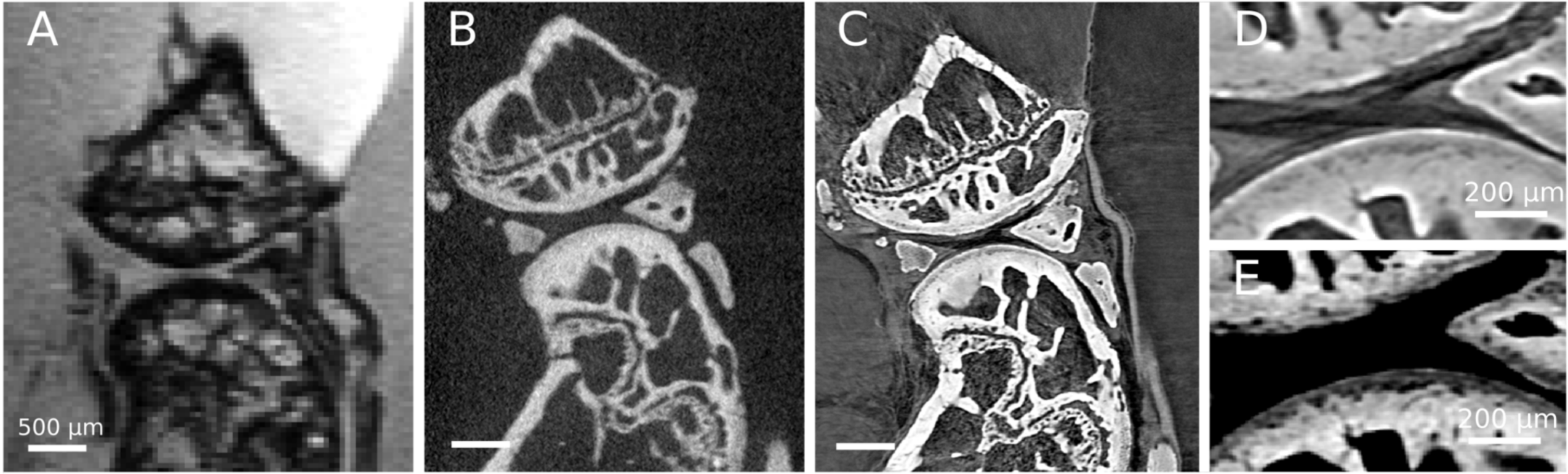
A
500 µm
B
C
D
200 µm
E
200 µm

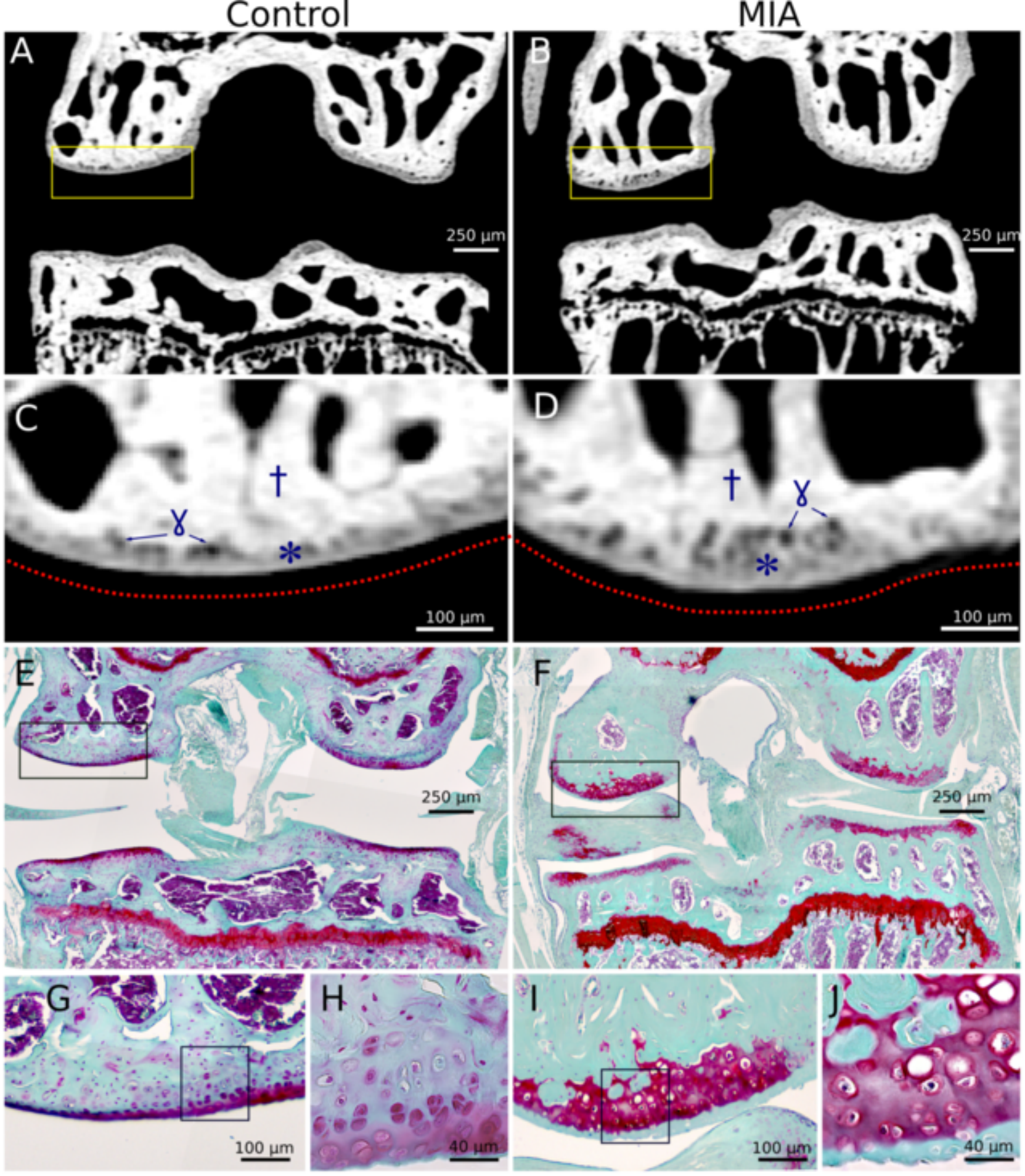
Control
MIA
A
B
250 µm
250 µm
C
D
100 µm
100 µm
E
F
250 µm
250 µm
G
H
I
J
100 µm
40 µm
100 µm
40 µm

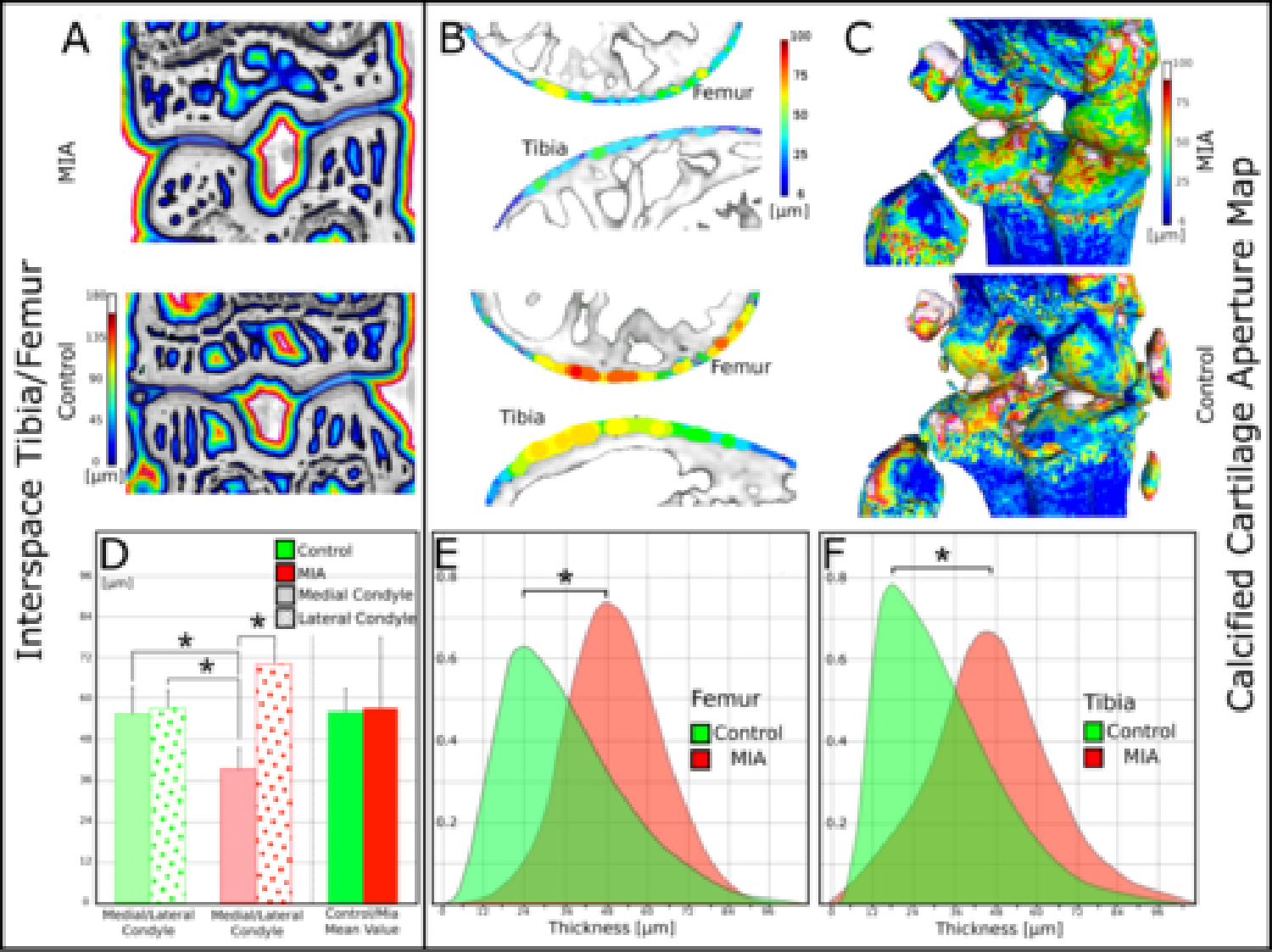
A
MIA
Control
[µm]
B
Femur
Tibia
[µm]
C
MIA
Control
Interspace Tibia/Femur
Calcified Cartilage Aperture Map
D
[µm]
Control
MIA
Medial Condyle
Lateral Condyle
Medial/Lateral Condyle
Medial/Lateral Condyle
Control/Mia Mean Value
E
Femur
Control
MIA
Thickness [µm]
F
Tibia
Control
MIA
Thickness [µm]

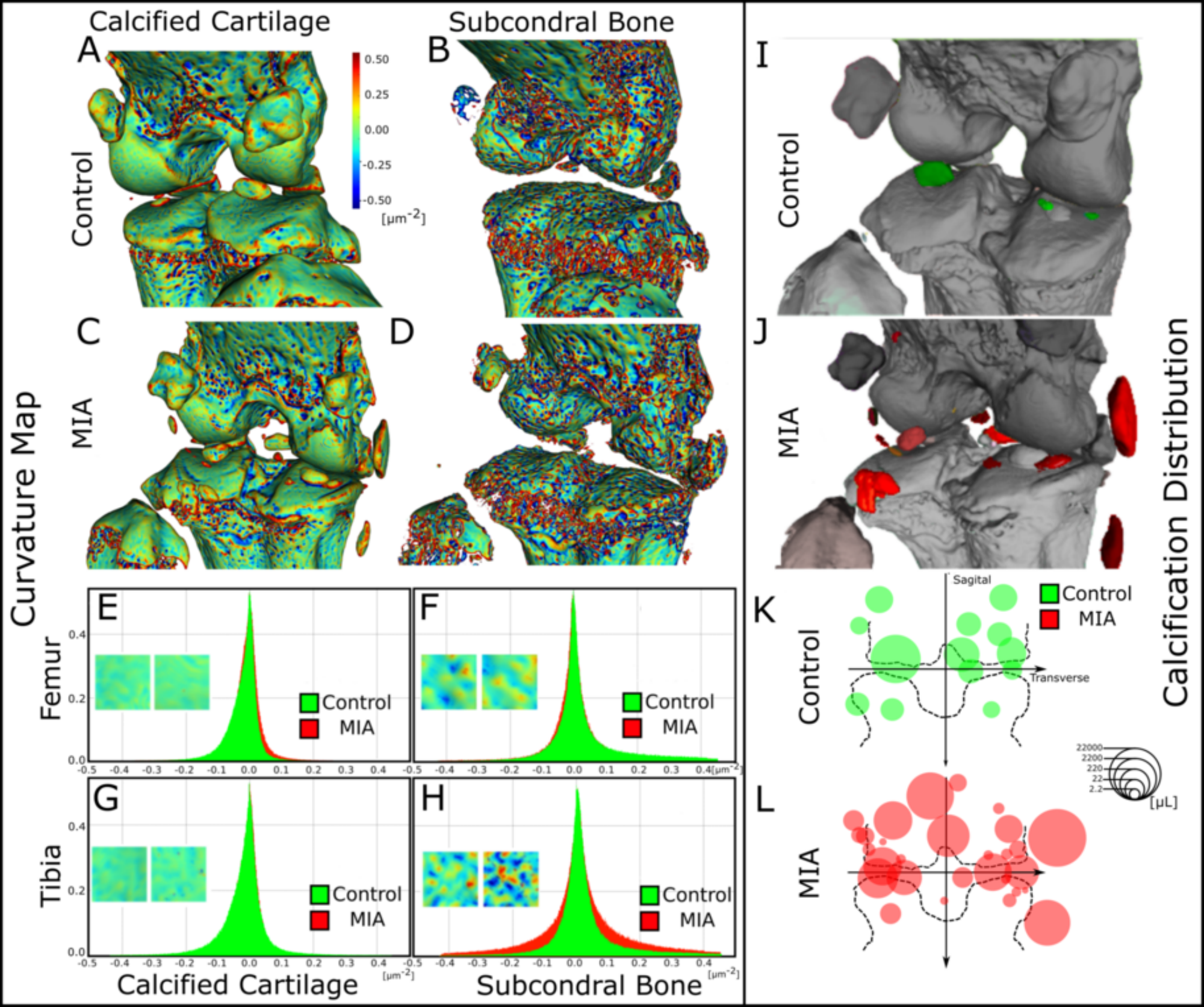
Curvature Map
Calcified Cartilage
Subcondral Bone
A
B
C
D
Control
MIA
0.50
0.25
0.00
-0.25
-0.50
[μm-2]
E
F
G
H
Femur
Tibia
Control
MIA
Calcified Cartilage
Subcondral Bone
[μm-2]
Calcification Distribution
I
J
K
L
Sagital
Transverse
22000
2200
220
22
2.2
[μL]

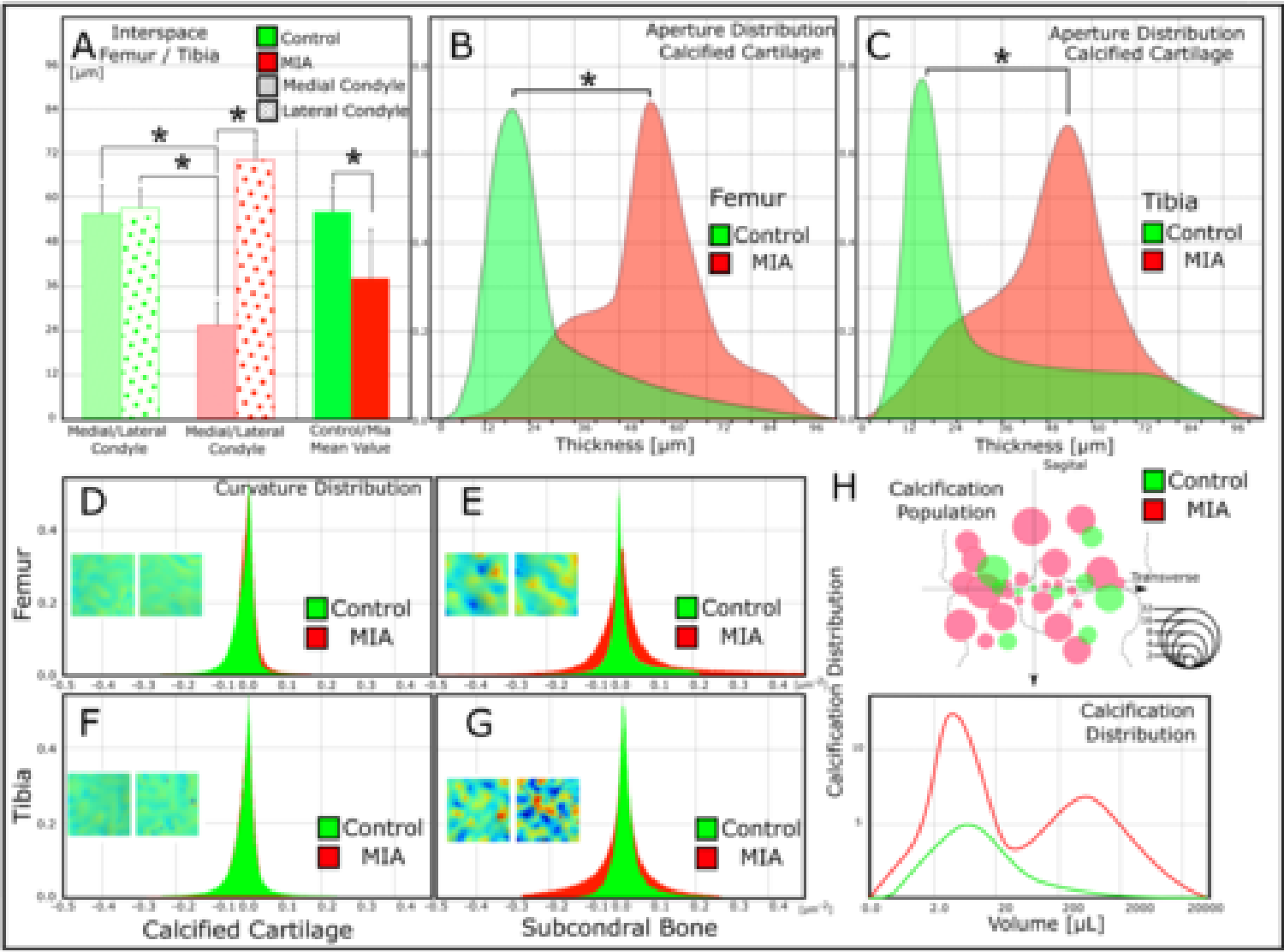
A
Interspace
Femur / Tibia
[µm]
Control
MIA
Medial Condyle
Lateral Condyle
Medial/Lateral Condyle
Medial/Lateral Condyle
Control/Mia Mean Value
B
Aperture Distribution
Calcified Cartilage
Femur
Control
MIA
Thickness [µm]
C
Aperture Distribution
Calcified Cartilage
Tibia
Control
MIA
Thickness [µm]
D
Curvature Distribution
Femur
Control
MIA
E
Control
MIA
F
Tibia
Control
MIA
Calcified Cartilage
G
Control
MIA
Subcondral Bone
H
Calcification Population
Sagital
Transverse
Control
MIA
Calcification Distribution
Calcification Distribution
Volume [µL]

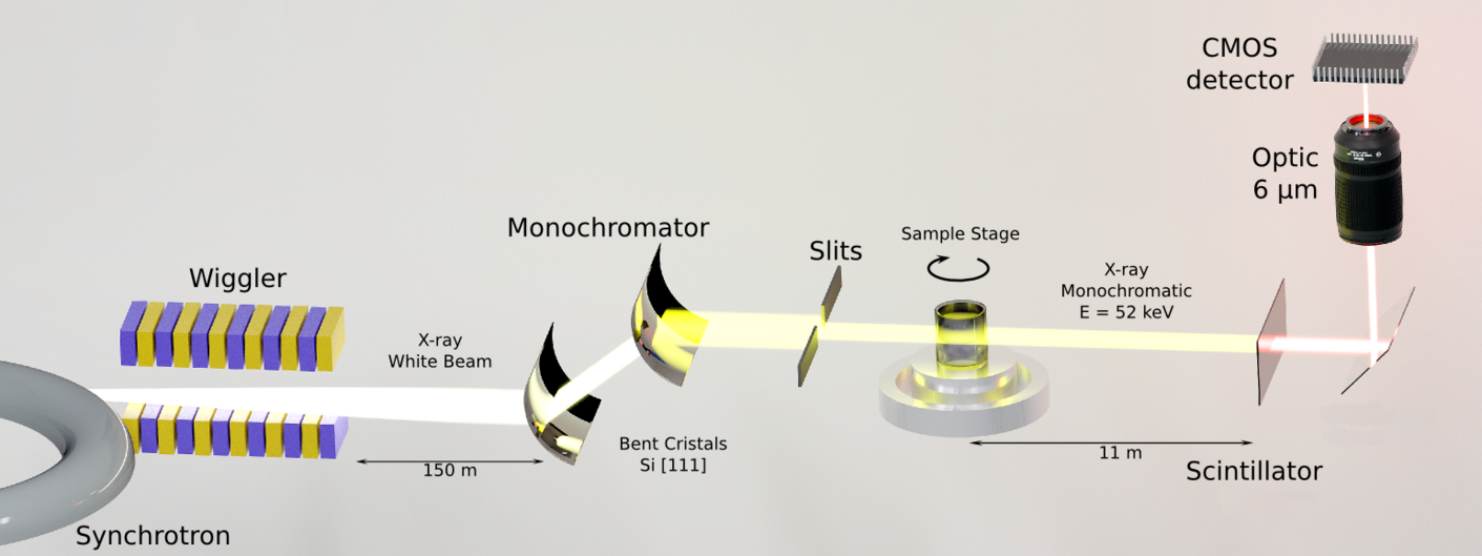
CMOS
detector
Optic
6 µm
Monochromator
Slits
Sample Stage
Wiggler
X-ray
White Beam
X-ray
Monochromatic
E = 52 keV
Bent Cristals
Si [111]
150 m
11 m
Scintillator
Synchrotron

Morphological Metrics			
	Control (n=6)	MIA (n=6)	p<0.01
$D_{BothCondyles}$ [μm]	56.3 ± 6.6	37.4 ± 13.9	
$D_{MedialCondyle}$ [μm]	55.6 ± 9.1	25.6 ± 6.8	* * *
$D_{LateralCondyle}$ [μm]	56.7 ± 4.1	70.7 ± 4.3	
T_{Femur} [$\mu\ m$]	24.2 ± 7.3	47,7±15.4	
T_{Tibia}[μm]	25.1 ± 8.1	44.4 ± 17.2	* *
$V_{CacifiedCartilage}$[μm]	5.84 ± 0.86	11.0 ± 2.45	*
C^{Femur} [mm^2] $^{Calci\,fied\,Cartilage}$	4.32 ± 1.09 × 10^{-2}	4.57 ± 1.72 × 10^{-2}	
C^{Tibia} [mm^2] $^{Calci\,fied\,Cartilage}$	4.75 ± 1.14 × 10^{-2}	4.81 ± 1.82 × 10^{-2}	
C^{Femur} [mm^2] $^{Subcondral\,Bone}$	6.78 ± 2.25 × 10^{-2}	12.7 ± 3.54 × 10^{-2}	* *
C^{Tibia} [mm^2] $^{Subcondral\,Bone}$	7.54 ± 2.47 × 10^{-2}	11.6 ± 2.85 × 10^{-2}	
$N_{Calcification}$	12.1 ± 4.21	54.8 ± 21.5	*
$V_{Calcification}$ [μL]	2.77 ± 0.462 × 10^3	3.70 ± 0.684 × 10^4	*

Table 1. All computed metrics on the knees database (control n= 6 and MIA n = 6). With D: Interspace the tibia and the femur; T : local thickness of the calcified cartilage; V : volume; C: Curvature of the specified surface; N: Number of calcification.Each $*$ a statistical difference in between the control and MIA group with p < 0.001